Journal Name

Dynamic Article Links ►

Cite this: DOI: 10.1039/c0xx00000x

www.rsc.org/xxxxxx

ARTICLE TYPE

In-situ synchrotron study of ordered (*P4$_3$32*) and disordered (*Fd*-3*m*) $LiMn_{1.5}Ni_{0.5}O_4$ as lithium ion battery cathode

Pushpaka B. Samarasingha*[a], Jonas Sottmann [a], Serena Margadonna [a], Ola Nilsen [a] and Helmer Fjellvåg [a]

Received (in XXX, XXX) Xth XXXXXXXXX 20XX, Accepted Xth XXXXXXXXX 20XX

DOI: 10.1039/b000000x

In-situ powder synchrotron diffraction and X-ray absorption spectroscopy have been used to investigate cation ordered as well as disordered modifications of the $LiMn_{1.5}Ni_{0.5}O_4$ spinel type compound as Li-ion battery (LIB) cathode material during electrochemical cycling. Their structural state depends on the adopted heat treatment conditions and is ascertained by Raman and neutron data. The degree (none, partial, complete) of Mn – Ni ordering is one parameter that influences the electrochemical behaviour. The in-situ data reveal significant differences in behaviour with respect to structural phase transitions and oxidation/charge state for the nickel atoms during electrochemical cycling. *Ordered* $Li_2Mn_3NiO_8$ undergoes two consecutive first order structural phase transitions between spinel type phases on charging/discharging, most probably connected with steps in oxidation state for the Ni-atoms as supported by XANES data. The disordered phase shows rather a smooth decrease in unit cell volume on charging. The situation appears dependent on any slight presence of $Li_xNi_{1-x}O$ impurities; a larger volume contraction is then followed by a small volume jump into a Ni(III) based spinel phase. In-situ XANES clearly support Ni(II), Ni(III) and Ni(IV) states for the three different phases of the ordered material. However, for none of the disordered phases XANES gave any indication for Ni(IV). Hence, for the fully charged disordered materials, the $Ni^{3+/4+}$ couple does not take part in the redox activity. Possible alternatives are overlapping of the $Ni^{4+/3+}$ and $Mn^{5+/4+}$ redox couples, however, future verification is required.

Key words

In-situ synchrotron, diffraction, XANES, lithium ion battery, cathode material.

1. INTRODUCTION

Spinel structured materials are of interest as cathodes for Li-ion batteries (LIB). Subsequent to early works on Li-incorporation in magnetite [1] the first reversible Li^+ intercalation was achieved for the $LiMn_2O_4$ spinel by the group of Goodenough in the early 1980ies [2,3]. At that time lithium ion battery researchers focused on batteries with cathode in its charged state. SONY Corporation designed an alternative Li-ion rechargeable battery with the cathode in the discharged state ($LiCoO_2$/graphite battery) [4,5] and studied $Li_{1-x}Mn_2O_4$ as a LIB cathode [6,7,8]. $Li_{1-x}Mn_2O_4$ has an open circuit voltage (V_{oc}) of about 4 V (vs. Li^+/Li) in contrast to the plateau at 3 V for $Li_{1+x}Mn_2O_4$. The $Li_{1-x}Mn_2O_4$ exhibits two distinguishable regions in its voltage vs *x* curve; first a 4.2 V plateau in the range $1 > x > 0.5$ and then a continuous gradual change at 4.0 V for $0.5 > x > 0$ [2]. The theoretical capacities of $Li_{1-x}Mn_2O_4$ and $Li_{1+x}Mn_2O_4$ spinels are limited to 0.5 Li per Mn (~147 mAh/g), however, this is within the practical capacity range of $LiCoO_2$ (~140 mAh/g). Spinels are interesting alternative cathodes based on inexpensive and environmentally benign elements.

$LiMn_{1.5}Ni_{0.5}O_4$ is derived from $LiMn_2O_4$ by substitution, and has gained attention due to higher gravimetric energy density and lower cost compared to $LiCoO_2$. For $LiMn_{1.5}Ni_{0.5}O_4$ the electrochemically active red-ox couple is $Ni^{2+/4+}$ [9], leading to a higher potential of ~ 4.7 V versus Li/Li^+. The gravimetric energy density is as high as ~700 Wh/kg. In $LiMn_{1.5}Ni_{0.5}O_4$ the redox couple during initial Li^+ removal is $Ni^{2+/3+}$, which Goodenough *et al.* [2] described to be pinned near the top of the O^{2-}:$2p^6$ band since the voltage change at $x = 0.5$ in $Li_{1-x}Mn_{1.5}Ni_{0.5}O_4$ is small [6]. For $x > 0.5$, the active redox couple is assumably $Ni^{4+/3+}$. However, this redox couple could possibly overlap with $Mn^{5+/4+}$ [2].

The structural and electrochemical properties of $LiMn_{1.5}Ni_{0.5}O_4$ depend strongly on synthesis routes and heat treatment conditions. Any presence of the impurity phase $Li_xNi_{1-x}O$ may lead to lower capacity due to parasitic loss of active material

[10,11].$LiMn_{1.5}Ni_{0.5}O_4$ may exist in two distinct forms; a Ni-Mn *ordered* phase (space group $P4_332$) and a Ni-Mn *disordered* phase (*Fd*-3*m*). The subtle difference in Mn and Ni scattering by X-rays makes their powder XRD patterns almost identical, and there is no larger difference in unit cell volume caused by the ordering process [12]. Differentiation between these two forms can conveniently be done by Raman spectroscopy (observation of different modes) or by powder neutron diffraction (strong Mn – Ni scattering contrast). Of these, the *disordered* phase has been widely studied, probably due to comparatively easy synthesis. According to Fang *et al.* [13] materials treated at 600 °C for > 8 h take the *ordered* structure. Likewise, Park *et al.* [9] and Wu *et al.* [14] report that a final treatment at 700 °C of samples originally treated at higher temperatures results in the *ordered* phase. This is contrasted by Feng *et al.* [12] who rather reported a *disordered* state for materials treated at 900 °C followed by a treatment at 700 °C. While most studies find the *disordered* phase to show the best electrochemical performance, Park *et al.* [9] and recently Wu *et al.* [14] report that the *ordered* phase has superior electrochemical properties. Our recent study [15] shows that treating the material at 600 °C for 20 h gives the *disordered* phase while the *ordered* phase is obtained after 20 h at 700 °C, even for samples initially treated at higher temperatures. Consistent with Park *et al.* [9] and Wu *et al.* [14] we find highest capacity for the *ordered* phase. According to Cai *et al.*[16] the majority of studies on electrochemical properties do not take into account the possibility of partial Ni/Mn ordering. On the other hand, the relevant studies of *e.g.* Kim *et al.* [17] and Shaju *et al.* [18] are based on X-ray diffraction, which is unsuitable for characterizing partial Ni/Mn distribution and also for distinguishing the *disordered* and *ordered* phase unless synchrotron powder X-ray diffraction data are at hand.

The current (*in-situ*) synchrotron study utilizes the same samples (or new batches thereof) as in our previous study of $LiMn_{1.5}Ni_{0.5}O_4$ [15] where Raman and neutron diffraction was used to distinguish *ordered* and *disordered* phases. Thereby *in-situ* electrochemical data can be directly connected with the structural state of the materials. Currently *in-situ* synchrotron powder diffraction is combined with absorption spectroscopy during electrochemical cycling. This allows us to describe changes in crystal structure (unit cell dimensions, symmetry) and in the oxidation states of nickel (and to some extent manganese) during stages of the charging and discharging cycles. This provides a quite complete picture of structural and electronic changes during electrochemical cycling of $LiMn_{1.5}Ni_{0.5}O_4$ as a LIB cathode material.

2. EXPERIMENTAL

2.1 Material synthesis and characterization

Powder samples of $LiMn_{1.5}Ni_{0.5}O_4$ were prepared according to the recipes in [15]. In brief, this involved seven steps: 1. metal nitrate mixing with ethylene glycol and citric acid monohydrate; 2. mixing for 20 h; 3. heating while mixing; 4. formation of viscous resin; 5. further heating; 6. ignite with sudden burst of particles; 7. post treatment of received material at selected temperatures. The studied samples are listed in Table 1.

Table 01 Naming of samples, annealing temperatures and holding times.

Sample tag	Treated at (°C)	Time (h)
Mn15-600_20h	600	20
Mn15-700_20h	700	20
Mn15-800_700	800 followed by 700	10 + 10
Mn15-900_700	900 followed by 700	10 +10
Mn15-1000_700	1000 followed by 700	10 +10
Mn15-900_60h	900	60

For the *in-situ* studies, see 2.2, optimized cathodes were prepared as described in [15], by mixing the oxide powder with [p(VdF-HFP)], Super P Carbon Black and Propylene carbonate (PC); blending the mixture with acetone and achieving a viscous suspension during stirring; casting the suspension onto a glass plate; before leaching the PC with ether and obtaining the final cathode tape to be investigated. The cathodes were assembled in a Swagelok type cell, designed for spectroscopic measurements in the transmission mode with metallic Li as anode. The electrolyte (Merck) was 1 M $LiPF_6$ in a 1:1 (weight ratio) ethylene carbonate : di-methyl carbonate (EC : DMC) mixture. The samples Mn15-600_20h, Mn15-900_700, and Mn15-900_60h were explored, Table 1.

2.2. In-situ synchrotron studies during electrochemical cycling

Regular room temperature synchrotron powder diffraction data were collected at the Swiss Norwegian Beam Lines, BM01A and BM01B at ESRF, Grenoble. The samples were kept in rotating 0.7 mm borosilicate capillaries, and either a Pilatus 2D detector (wavelength λ = 0.70135 Å) or a high resolution analyser crystal detector was used. The Pilatus detector was calibrated by means of a LaB_6 standard. The wavelength (λ = 0.50480 Å) used for the high resolution analyser crystal detector (BM01B) was determined from measurements of a Si NIST standard. All profile fittings and Rietveld refinements were performed using the General Structure Analysis Suite (GSAS) with the EXPGUI [19] interface or TOPAS academic.

In-situ galvanostatic charge-discharge experiments were performed using an Astrol BAT-SMALL battery tester. The cells were cycled between 3.0 and 4.9 V at room temperature (20 ^{0}C). *In-situ* XRD and XAS data were collected simultaneously at BM01B. Room temperature Ni K-edge and Mn K-edge X-ray Absorption Near Edge spectroscopy (XANES) were collected for Mn15-600_20h, Mn15-900_700, and Mn15-900_60h samples in transmission mode, and MnO, Mn_2O_3, MnO_2, $NiCl_2$, NiO and $LaNiO_3$ were used as standards. Collection on *in-situ* data at during cycling of the materials in the battery cell was not feasible for the Mn K-edge, owing to high absorption at low photon energies. X-ray Absorption Fine Structure spectroscopy (EXAFS)

spectra were collected at the Ni K-edge for the Mn15-900_700 sample.

3. RESULTS AND DISCUSSION

3.1 Phase analysis, structural state of the cathode materials at ambient

All samples are single phase according to home-lab powder X-ray diffraction analyses [15] (Bruker D8, reflection geometry, CuKα_1-radiation, Lynxeye detector). Raman and powder neutron diffraction data [15] show that the Mn-Ni *ordered* $P4_332$ polymorph is obtained for all samples with an annealing at 700 °C, see Table 1, whereas the *disordered* (*Fd-3m*) polymorph is obtained at 600 °C. The current Mn15-600_20h and Mn15-900_700 samples are identical to those investigated by powder neutron diffraction (PND) in Ref. [15]. It is interesting to note that the superior signal-to-noise ratio of instrumentation at BM01A, ESRF, reveals features that escape detection in the home laboratory. The synchrotron diffraction data (PXRD, λ= 0.50480 Å, capillaries and HR detector, BM01B) confirms Mn15-600_20h as phase pure, however, the other samples contain 1-5 % of the $Li_xNi_{1-x}O$ rock salt type impurity phase, most for the Mn15-900_60h sample (~ 5 %). Hence, literature claims on phase-purity from home-lab data must be judged in this perspective.

The excellent signal-to-noise ratio of the Pilatus detector allows detection of superstructure reflections (↓) caused by to Mn/Ni ordering in the Mn15-900_700, Figure 1 left, in full agreement with Raman [15] and powder neutron diffraction data (the latter are included in Figure 1, right). Corresponding Pilatus data show that Mn15-600_20h and Mn15-900_60h are *disordered* spinels, space group *Fd-3m*. Also shown in Figure 1 are additional weak peaks (*) in the patterns for Mn15-900-60h and Mn15-900_700. Precipitation of small amounts (~ 5 %) of the $Li_xNi_{1-x}O$ impurity obviously occurs on prolonged holding time at 900 °C.

Cai *et al* [16] reported that the rock salt impurity $Li_xNi_{1-x}O$ starts to precipitate on holding at temperatures >700 °C, but reverts back into the spinel phase when the temperature is lowered. The disordered Mn15-600_20h sample does not contain this impurity (Figure 1). Hence, one may wonder whether $Li_xNi_{1-x}O$ takes a role in the cation ordering process, for instance that nickel is shuffled via the impurity phase in addition to move by diffusion processes.

The Mn15-900_700, Mn15-900_60h and Mn15-600_20h samples were selected for further analysis and *in-situ* studies. Assessment of the oxidation states of Ni and Mn was performed by measuring Mn and Ni K-edge XANES data, prior to the cathode preparation. All three samples show identical Mn K-edge spectra (Figure S1) and Ni K-edge spectra (Figure S2). The edge positions for the spectra suggest that the oxidation state of Mn is between +III and +IV while that of Ni is very close to +II in all the as-prepared materials.

3.2 Electrochemical prescreening of laboratory coin cells

Electrochemical properties of the current cathode materials were reported in Ref. 15 based on laboratory coin cell studies. Here, we provide some additional details of relevance for the synchrotron *in-situ* studies. Figure 2 compares voltage plateaus for *disordered* and *ordered* samples, subjected to different annealing conditions. The plateau at some 4.7 V represents the $Ni^{2+/3+}$ and $Ni^{3+/4+}$ redox couples. Certain detailed features are reported to differ between the *ordered* and *disordered* phases by Kim *et al.* [17] and Lee *et al.* [20]; a splitting of the plateau into two separate plateaus separated by > 50 mV occurs typically for the *disordered* phase [21], whereas the separation shrinks to 30 mV or is virtually undistinguishable for the *ordered* phase. The situation appears not fully clear, since Cabana *et al.* [20] found a separation of 60 mV for the *ordered* phase and indicated that close to ideal Ni-Mn ordering is required for a smaller separation of the two plateaus.

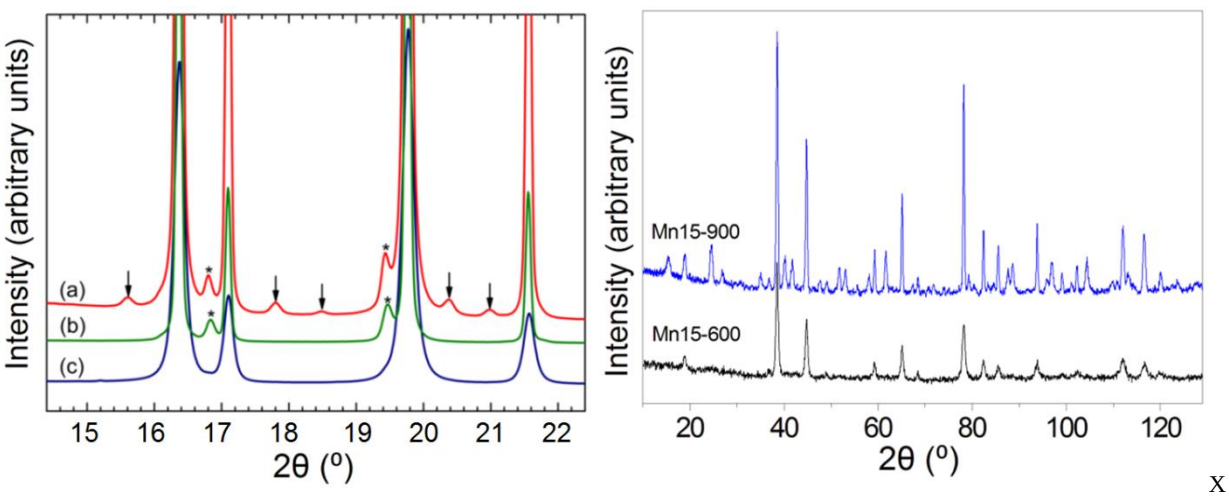

X

Fig.01/ ***Left****: PXRD (λ = 0.70135 Å, capillaries and Pilatus detector) patterns of (a)Mn15-900_700, (b)Mn15-900_60h, (c)Mn15-600_20h; superstructure reflections (↓), impurity reflections (*);* ***Right****: Powder neutron diffraction (PND, λ = 1.5560 Å) profiles showing major differences in diffraction profiles upon Mn-Ni cation ordering; space groups $P4_332$ (ordered) and Fd-3 (disordered).*

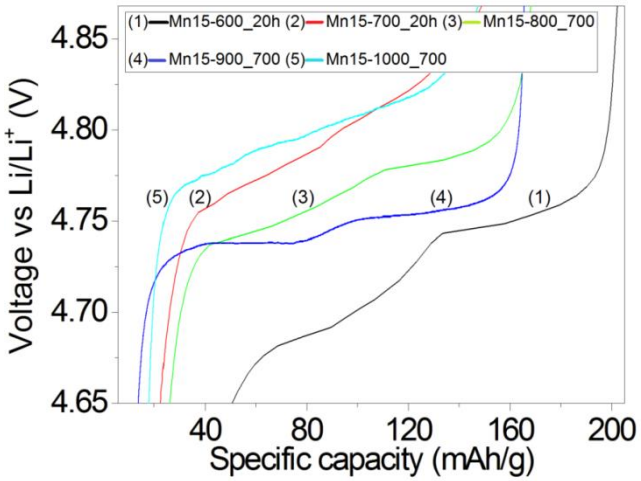

Fig.02/1st charge curves of $LiMn_{1.5}Ni_{0.5}O_4$/ Li cells for the 4.65 - 4.85V range

The observed plateau separations are listed in Table 2. A wide separation for the *disordered* phase is fully consistent with our Raman, neutron and synchrotron characterization data. The voltage range for the $Ni^{4+/3+}$ redox couple may overlap with the $Mn^{5+/4+}$ redox couple[2]. This could possibly influence the plateau separation. To our knowledge no experimental data exist to (dis)prove $Mn^{5+/4+}$. The current *in-situ* study is inconclusive since measurements at the Mn-edge are hampered by severe cell and sample absorption.

Table 02 Plateau separation from electrochemical experiments of $LiMn_{1.5}Ni_{0.5}O_4$/ Li cells (1st charge cycle).

Sample	[a] Separation at $Ni^{2+/3+}$ - $Ni^{3+/4+}$	Structural state
Mn15-600_20h	~ 70 mV	*Disordered*
Mn15-700_20h	Not clear	*Ordered*
Mn15-800_700	~ 20 mV	*Ordered*
Mn15-900_700	~ 15 mV	*Ordered*
Mn15-1000_700	Not clear	*Ordered*

[a] Values obtained based on our previous study [15]

3.3 In-situ synchrotron diffraction studies during battery cycling

3.3.1. Ordered Mn15-900_700, diffraction and XANES study at the Ni K-edge

The theoretical capacity for the ordered $LiMn_{1.5}Ni_{0.5}O_4$ material ($Li_2Mn_3NiO_8$) is 147 mAh/g. The electrochemical cell was initially charged at I = 0.02 mA, thereafter at 0.0855 mA, as marked on Figure 3(a). *In-situ* XRD (λ = 0.50480 Å; transmission mode) and XANES were recorded at the stages indicated in Figure 3(b). The diffraction data for the first charging cycle shows two phase transitions, cubic phase I to cubic phase II and cubic phase II to cubic phase III, see the 2D diffraction patterns in Figure 4(a). The intensity pattern is basically unchanged and all the involved phases are hence of the spinel type. Both transitions are connected with volume jumps, proving their 1.order nature [see inset, Figure 4 (a)]. The transitions are sluggish with respect to the variation in Li-content during the electrochemical reactions. Hence, regions are clearly visible proving the coexistence of two phases over wider Li-content intervals. The transitions are fully reversible during recharging, and the structural behaviour remains similar for all five cycles.

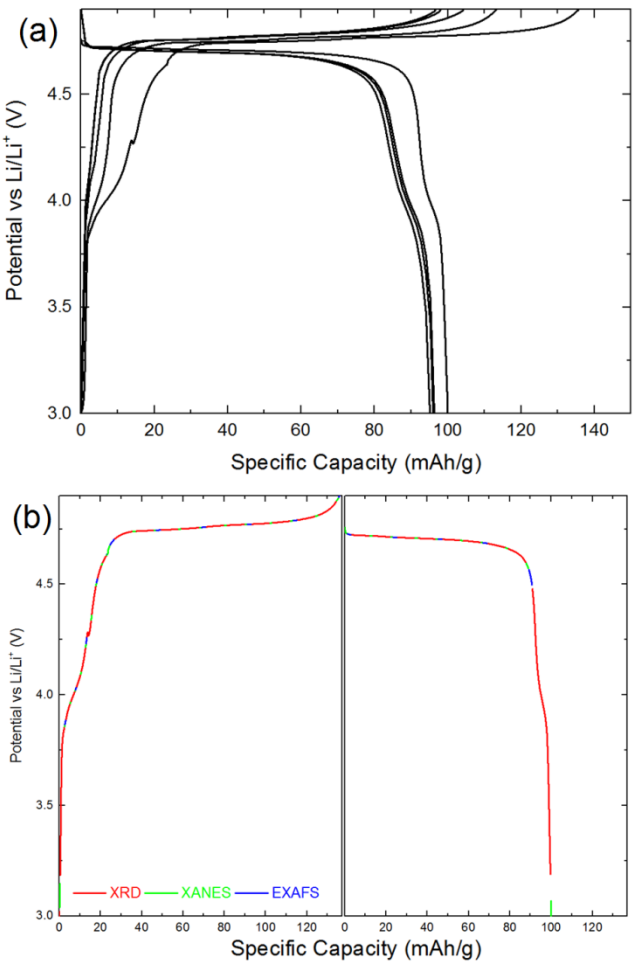

Fig.03/ Mn15-900_700: **(a)** first 5 galvanostatic cycles in the in-situ cell, **(b)** marked stages at which XRD and XANES data were collected.

The respective unit cell dimensions of the three cubic phases are shown in Figure 4(b). The integrated intensities for selected Bragg reflections versus capacity for each of the phases are shown in Figure 5. The cubic phases span different ranges during the cycling. The situation remains fully reversible during all five galvanostatic charge - discharge cycles. Data for the first and fifth cycle are compared in Figure S3. Mukerjee *et al.* [22] reported that this type of phase transition in $LiMn_2O_4$ spinel goes via additional phases as based on XRD. We see, however, no indications for any additional phases in the synchrotron patterns. We note, that

the initial charging (removal of Li-atoms) leads to a small, continuous shortening of the *a*-axis, where after *a*(I) remains constant. This variation is fully reversible during charge and discharge cycles.

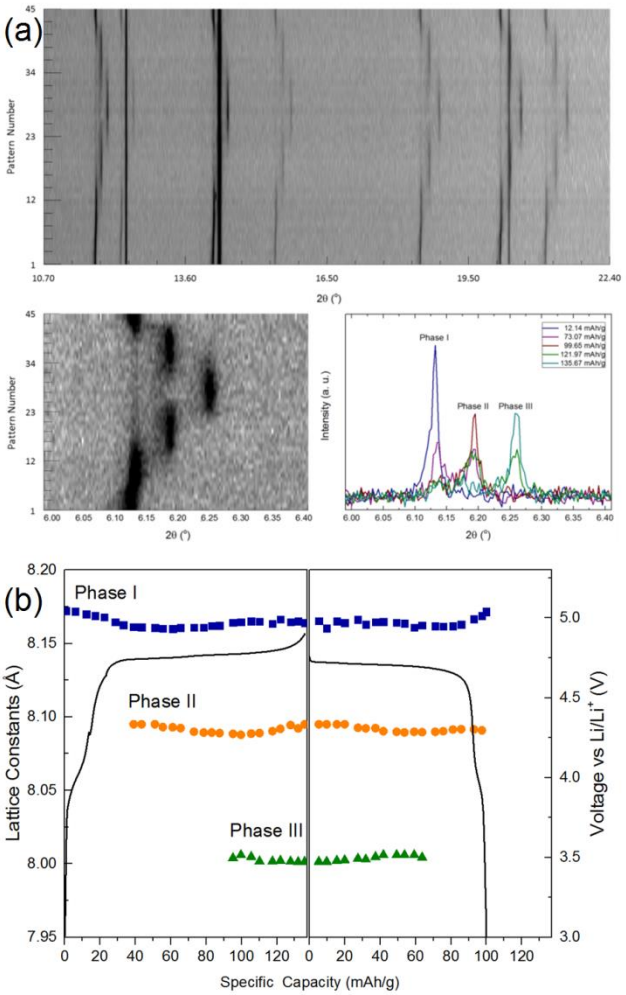

Fig.04/2D projection of consecutive in-situ XRD patterns for Mn15-900_700 during first charge cycle for 3.0-4.9 V region; **(a)** XRD (λ = 0.50480 Å) profile in the 10.7–22.4 ° 2θ range, left bottom inset shows the (111) reflection, right bottom inset depicts the diffraction patterns **(b)** the corresponding variation of unit cell dimensions versus capacity.

One may speculate whether this change is caused by Mn-oxidation, whereas phase II and III occur due to electronic changes for the Ni-atoms. The unit cell dimensions *a*(II) and *a*(III) are constant within their (capacity/Li-content) existence ranges, and the variable capacity is delivered through a continuous variation in mass fractions of the involved phases. Ideally, a maximum of two phases should be involved at any given charge situation. However, a careful inspection of the 2D diffraction patterns reveals that small amounts of phase-I remains when the phase fraction is dominated by phase-II and –III. It is likely that this reflects particles that are not electrochemically active; they have lost their connection to the electric conducting system. The composition $Li_{1-x}Mn_{1.5}Ni_{0.5}O_4$ is allocated to phase-II based on the charge state at maximum diffraction intensity, Figure 5. Phase-III is most likely completely delithiated $Mn_{1.5}Ni_{0.5}O_4$. Choi *et al.* [23] also report such co-existence of two phases. The unit cell dimensions for the initial $Li_2Mn_3NiO_8$ phase ($LiMn_{1.5}Ni_{0.5}O_4$) a = 8.160 Å, are shortened and are for the partly charged $Li_{2-x}Mn_3NiO_8$ phase a = 8.095 Å, whereas for the fully charged state a = 8.005 Å. This is consistent with the smaller ionic radius of Ni^{4+} relative to Ni^{3+} and Ni^{2+}. The consecutive phase transitions occur in the voltage region 4.5-4.9 V where $Ni^{2+}/Ni^{3+}/Ni^{4+}$ oxidation/reduction takes place. Therefore, the cubic phases I, II and III are assigned to spinel structures with Ni^{2+}, $Ni^{3+}$and Ni^{4+}, respectively.

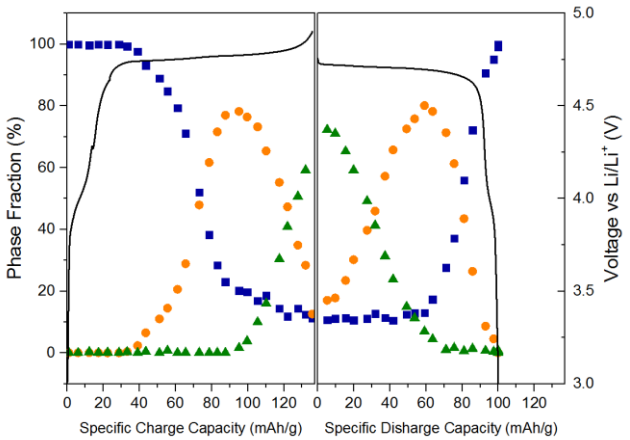

Fig.05/ Phase fraction during the first charge-discharge cycle; phase I (■), phase II (●), phase III (▲).

In the XANES data, the Ni-edge shifts smoothly consistent with continuous change in the relative amounts of $Ni^{2+}/Ni^{3+}/Ni^{4+}$ cations in the cathode materials, see Figure 6. The studies show that the changes in the Ni oxidation states are fully reversible.

The XANES spectra for the three cubic phases at their maximal phase fraction are shown in Figure S4. The Ni K-edge of phase-II corresponds within ~2 eV with the $LaNiO_3$ Ni(III) standard, Figure 7. Ni(III) has d^7 electron configuration, expectedly Jahn Teller distorted if prevailing in low-spin state. On the average, the crystal structure remains cubic, however, at the local level EXAFS data gives hints for 4+2 distortions. The Ni-EXAFS data (Figure S5) shows major differences for phase-II relative to phase I and –III. This gives support to the potential Jahn Teller distortion of Ni(III), since Ni(II) in octahedral environment is d^8 ion normally with quite equal Ni-O bond distances, and Ni(IV) is formally a d^6 ion, also with expected regular octahedral geometry.

3.3.2. In-situ diffraction and XANES data at the Ni K-edge for the disordered phase

The Mn15-900_60h and Mn15-600_20h samples represent *disordered* spinels (*Fd-3m*). Their electrochemical behavior is quite similar, as well are the structural and electronic changes during charge and discharge, as seen by synchrotron powder diffraction and Ni-XANES data. Below, the focus is put on the phase pure Mn15-600_20h sample during its first (I = 0.087 mA;

rate C/8) and fifth (I = 0.353 mA; rate C/2) charging cycle. Interestingly, for this *disordered* sample there are no distinct phase transitions during charging as observed for the *ordered* $Li_{2-x}Mn_3NiO_8$ phase, as evident from comparison of Figures 4 and 8.

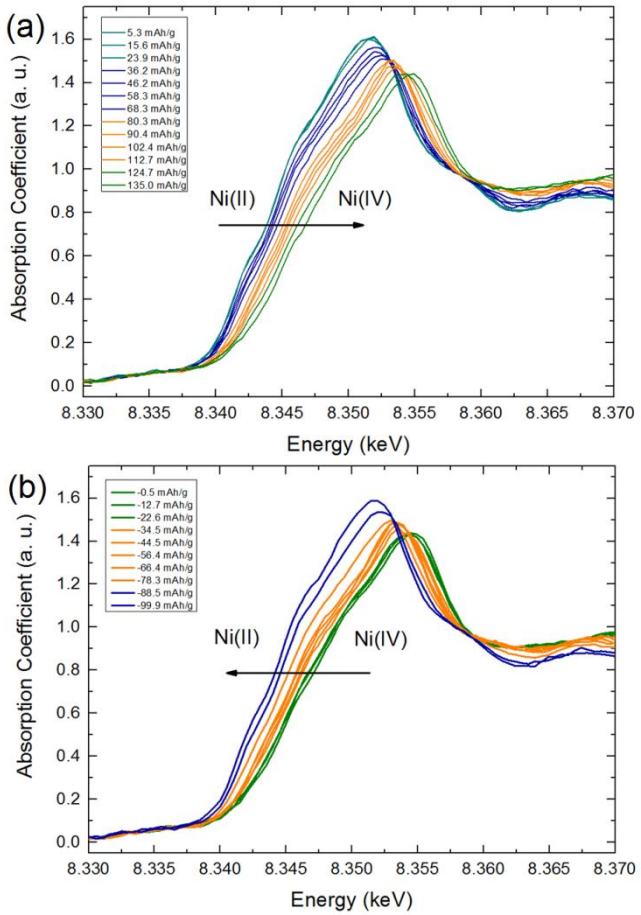

Fig.06/ In-situ XANES spectra of Mn15-900_700 **(a)** first charge step, **(b)** first discharge step.

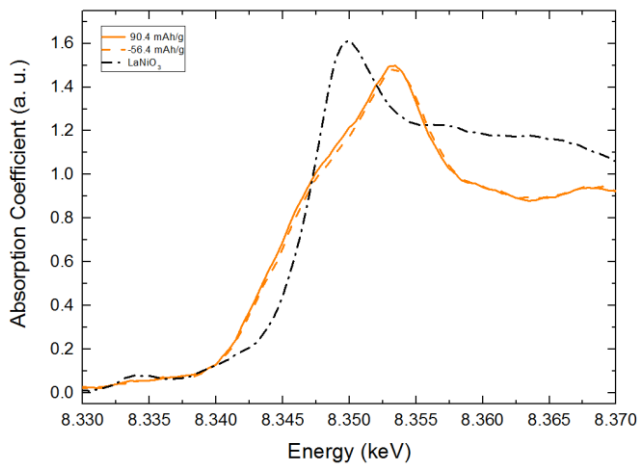

Fig.07/ In-situ XANES spectra (Ni K-edge) of Mn15-900_700 at the maximal phase fraction of cubic phase II during electrochemical cycling; comparison with the Ni(III) standard $LaNiO_3$.

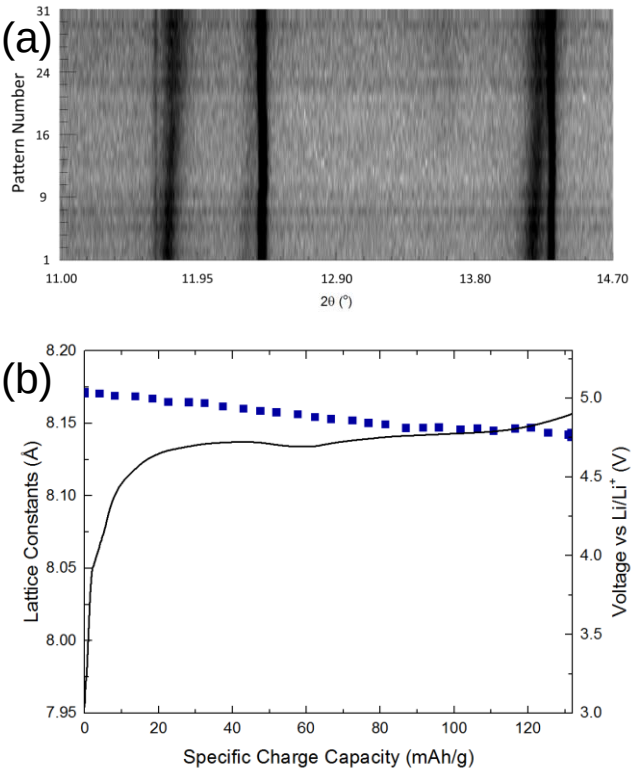

Fig.08/2D projection of consecutive in-situ XRD patterns for Mn15-600_20h during first charge step for the 3.0 - 4.9 V region; **(a)** XRD (λ = 0.50480 Å) profile in the 11–14.7 ° 2θ range, **(b)** the corresponding lattice parameter vs. capacity plot.

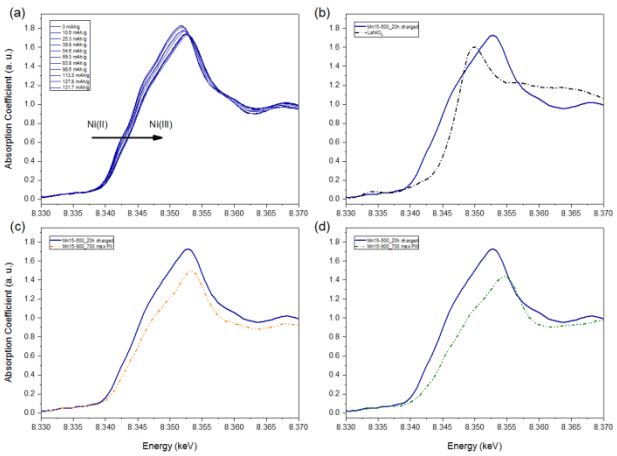

Fig.09/ In-situ XANES spectra (Ni K-edge) of Mn15-600_20h after completed first charge step; **(a)**beginning to end, **(b)**compared to Ni^{3+} standard, $LaNiO_3$ **(c)**compared to maximal phase fraction of cubic phase II of Mn15-900_700, **(d)**compared to end of charge step of sample Mn15-900_700.

Obviously the random distribution of the Ni-species on the octahedral sites prevents the first order transition connected with the charge states of the Ni-atoms. Instead a continuous decrease in unit cell dimensions is observed. During the complete charging process, the unit cell dimension for Mn15-600_20h contracts from 8.167 to 8.135 Å, i.e. by ~ 0.4 %, which is far less than what

is observed for the *ordered* phase, ~ 2 %.

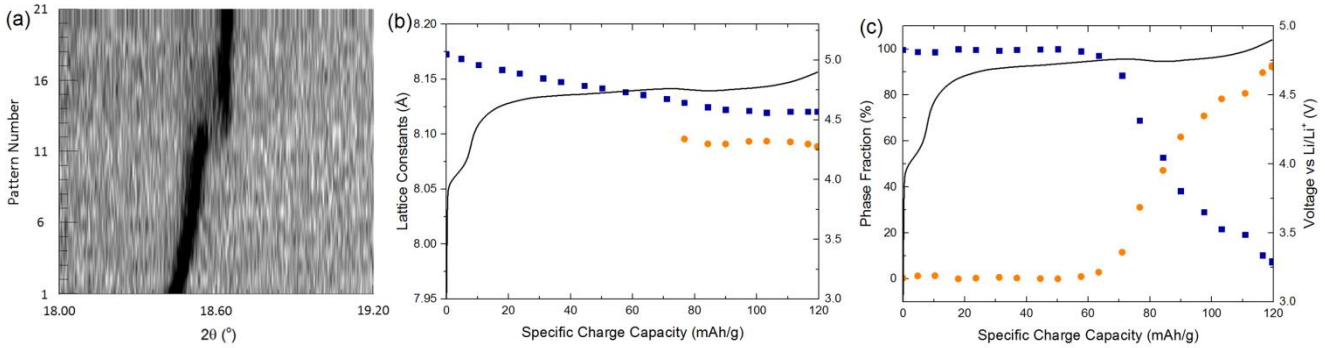

Fig.10/2D projection of consecutive in-situ XRD patterns for Mn15-900_60h during first charge step for 3.0-4.9 V region; **(a)** XRD (λ = 0.50480 Å) profile, **(b)** the corresponding lattice parameter vs. capacity plot, **(c)**change of phase fraction; cubic phase I (■)cubic phase II (●).

Neither the XAS spectra show the same clear change as for the *ordered* phase. This is reasonable since that the material as such is unable to undergo the first order structural transitions which appear to be ruled by the Ni-atoms at the *ordered* sites.

In-situ Ni K-edge spectra suggest that the Ni oxidation state of the *disordered* phase changes only from +2 to +3 after complete charging, see Figure 9. After completing the charge step the Ni-edge is comparable to that of the Ni^{3+}standard ($LaNiO_3$) within ~ 2 eV, Figure 9(b). The spectrum is identical to that for the maximal phase fraction of the cubic phase-II of Mn15-900_700, Figure 9(c), whereas it clearly differ from the Ni(IV) end of the charging stage of Mn15-900_700, Figure 9(d). Hence, these *in-situ* XANES spectra indicate that the $Ni^{3+/4+}$ step is missing.

The behavior depends surprisingly closely on details connected with sample composition and cation distribution. Notably, the *disordered* Mn15-600_20h does not show any phase transition during the charging step, however, the *disordered* Mn15-900_60h that contains a minor $Li_xNi_{1-x}O$ rock salt type impurity shows one distinct phase transition during the charging step, Figure 10. The new phase, with higher Ni-oxidation state, has a unit cell volume comparable to that of phase-II for the *ordered* phase. However, the volume jump is much less since the *a*-axis of phase-I for *disordered* Mn15-900_60h continues to decrease upon charging, while it saturated at a high constant value for the *ordered* phase, see Figure 4. The variation in phase fractions versus capacity is included in Figure 10. The *in-situ* Ni K-edge spectra shows similar behaviours as described for Mn15-600_20h. The oxidation state of nickel changes from +II to +III after complete charging, Figure 11. For both the *disordered* spinel samples, it appears that nickel does not convert into Ni(IV) at full charging. One alternative could be higher charged Mn-species, Mn(IV)/Mn(V) redox couples. Unfortunately, no XANES data were available for the Mn-edge with the current set-up. Finally, one may speculate whether the Ni(IV) state is masked in the sense that the additional charge is rather located as a hole in a band of O-dominant character, and thereby escapes detection. If so, the electronic structure of the *disordered* and *ordered* spinels differ significantly, which ought to be evaluated by first principles DFT calculations.

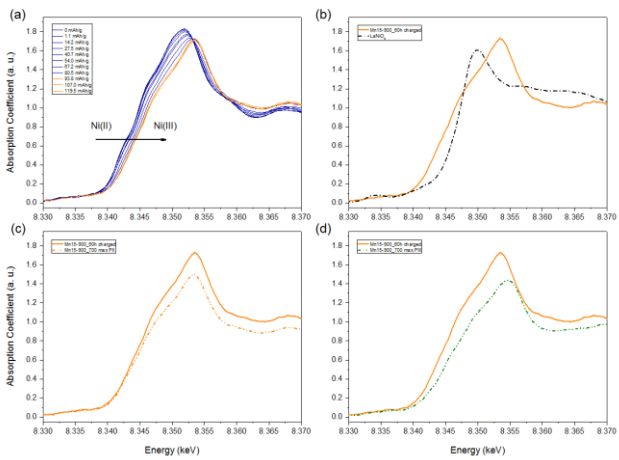

Fig.11/ In-situ XANES spectra (Ni K-edge) of Mn15-900_60h after completed first charge step; **(a)** beginning to end, **(b)** compared to Ni^{3+} standard, $LaNiO_3$ **(c)** compared to maximal phase fraction of cubic phase II of Mn15-900_700, **(d)** compared to end of charge step of Mn15-900_700.

CONCLUSIONS

Raman, powder neutron diffraction along with synchrotron powder diffraction provides required means to describe cation ordering in $LiMn_{1.5}Ni_{0.5}O_4$ spinel type cathode materials for LIBs, and in addition clarify the possible existence of minor amounts of impurity phases that escapes detection with conventional X-ray diffraction in the home laboratory. Variously synthesized and annealed samples of $LiMn_{1.5}Ni_{0.5}O_4$ show some differences in electrochemical behaviour, which ought to be explained in terms of chemical differences of the samples. The degree (none, partial, complete) of Mn-Ni ordering is one such parameter. Currently, well characterized samples with respect to such cation ordering as well with respect to presence or absence of minor amounts of $Li_xNi_{1-x}O$ impurities have been investigated

in-situ during electrochemical cycling by means of synchrotron powder diffraction and XAS studies. Significant differences in behaviour with respect to structural phase transition and oxidation/charge state for the nickel atoms are revealed. The *ordered* material undergoes two consecutive first order structural phase transition between spinel type phases, most probably connected with steps in oxidation state for the Ni-atoms as supported by XANES data. The fully disordered phase shows on the other hand a smooth decrease in the unit cell volume on charging (Li-removal). For a *disordered* sample with slight amounts of $Li_xNi_{1-x}O$ impurities, the situation is different; a larger volume contraction is followed by a small volume jump into a Ni(III) based spinel phase. Notably, for none of the disordered phases XANES gave any indication for Ni(IV). Hence, for the fully charged disordered materials, the $Ni^{3+/4+}$ couple does not take part in the redox activity. Other options are discussed above, however, these require future verification in terms of XANES data for Mn and O.

Notes and references

[a] *Department of Chemistry, Center for Materials Science and Nano Technology, University of Oslo, P.O.Box 1033, N-0315 Oslo, Norway*

Email: pushpaka.samarasingha@kjemi.uio.no, helmer.fjellvag@kjemi.uio.no*

† Electronic Supplementary Information (ESI) available: [extra Figures are supplied as supplementry Figures, numbered as Sx, x being the suplementary figure number]. See DOI: 10.1039/b000000x/

Acknowledgements

The authors thank the SNBL staff for their skilful assistance.

References

[1]. J.B. Goodenough, Y. Kim, *Chem. Mater.*, 2010, 22, 587.
[2]. M.M. Thackeray, W.I.F. David, P.G. Bruce, and J.B. Goodenough, *Mater. Res. Bull.*, 1983,18, 461.
[3]. W.I.F. David, M.M. Thackeray, L.A. De Picciotto, J.B. Goodenough, *J. Solid State Chemistry*, 1987, 67, 316.
[4]. A.P. Johnson, C.R. Schlaikjer, *J. Power Sources*, 1997, 68, 402.
[5]. K. Ozawa, *Solid State Ionics* 1994, *69*, 212.
[6]. J.M. Tarascon, D. Guyomard, *Electrochim. Acta*, 1993, 38, 1221.
[7]. D. Guyomard, J.M. Tarascon, *Solid State Ionics*, 1994, 69, 222.
[8]. M.M. Thackeray, P.J. Johnson, L.A. De Picciotto, P.G. Bruce, J.B. Goodenough, , *Mater. Res. Bull.*, 1984, 19, 179.
[9]. S.H. Park, S.W. Oh, S.H. Kang, I. Belharouak, K. Amine, Y.K. Sun, *Electrochimica Acta*, 2007, 52, 7226.
[10]. H.-S. Fang, Z.-x.Wang, X.-h. Li, H.-j. Guo, W.-j. Peng, *J. Power Sources*, 2006, 153, 174.
[11]. R. Alcantara, M. Jaraba, P. Lavela, J.L. Tirado, *Electrochimica Acta*, 2002, 47, 1829.
[12]. X.Y. Feng, C. Shen, X. Fang, C.H. Chen, *J. Alloys and Compounds*, 2011, 509, 3623.
[13]. H. Fang, Z. Wang, B. Zhang, X. Li and G. Li, *Electrochem. Commun.*, 2007, 9, 1077.
[14]. W.W. Wu, H.F. Xiang, G.B. Zhong , W. Su, W. Tang, Y. Zhang, Y. Yu, C.H. Chen, *Electrochimica Acta*, 2014, 119, 206.
[15]. P. B. Samarasingha, N.H. Andersen, M. Sørby, S. Kumar, O. Nilsen, H. Fjellvåg, **manuscript [paper I].**
[16] . L. Cai, Z. Liu, K. An, C. Liang *J. Mater. Chem. A*, 2013, 1, 6908.
[17] . J. H. Kim, S. T. Myung, C. S. Yoon, S. G. Kang and Y. K. Sun, *Chem. Mater*., 2004, 16, 906.
[18]. K. M. Shaju, P. G. Bruce, *Dalton Trans.*, 2008, 5471.
[19]. A. C. Larson and R. B. Von Dreele, *Los Alamos National Laboratory report*, 2004, *LAUR*, 86-748.
[20]. E. Lee, K. A. Persson, *Energy Environ. Sci.*, 2012, 5, 6047.
[21]. J. Cabana, M. Casas-Cabanas, F.O. Omenya, N.A. Chernova, M.S. Whittingham, C.P. Grey, *Chem. Mater.*,2012, 24, 2952.
[22]. S. Mukerjee, T.R. Thurston, N.M. Jisrawi, X.Q. Yang, J. McBreen, M.L. Daroux, X.K. Xing, *J. Electrochem. Soc.*, 1998,145, 466.
[23]. Sol Choi, JeongBae Yoon, Shoaib Muhammad, and Won-Sub Yoon, *J. Electrochemical Science and Technology*, 2013, 4, 34.

SUPPLEMENTARY INFORMATION

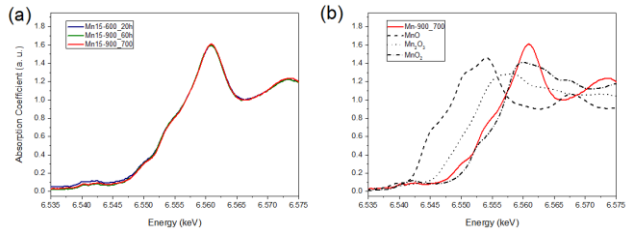

Fig.S1/ XANES at Mn K-edge for powder samples **(a)**Mn15-900_700, Mn15-900_60h, and Mn15-600_20h **(b)** Mn15-900_700 with standards; MnO, MnO_2, Mn_2O_3.

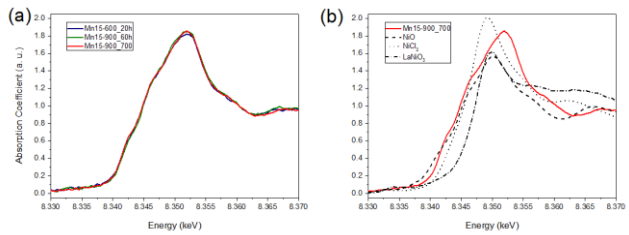

Fig.S2/ XANES at Ni K-edge for powder samples **(a)**Mn15-900_700, Mn15-900_60h, and Mn15-600_20h **(b)** Mn15-900_700 with standards; $NiCl_2$,NiO and $LaNiO_3$.

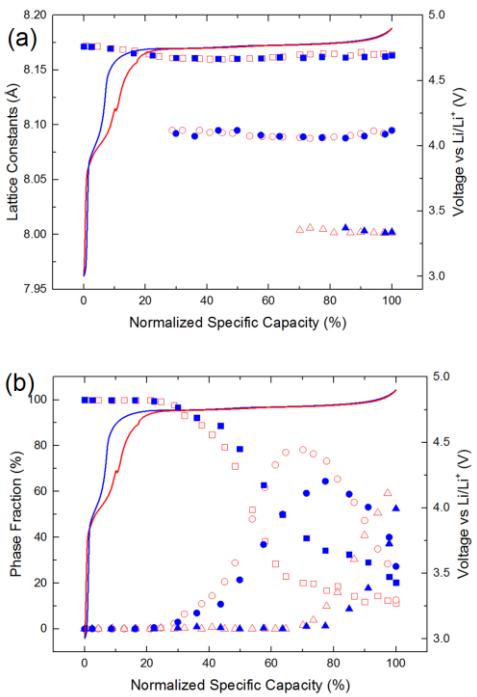

Fig.S3/ The first (red colour) and fifth (blue colour) charge steps of sample Mn15-900_700 **(a)** variation of unit cell dimensions, **(b)** variation of phase fractions for phase-I, -II and –III.

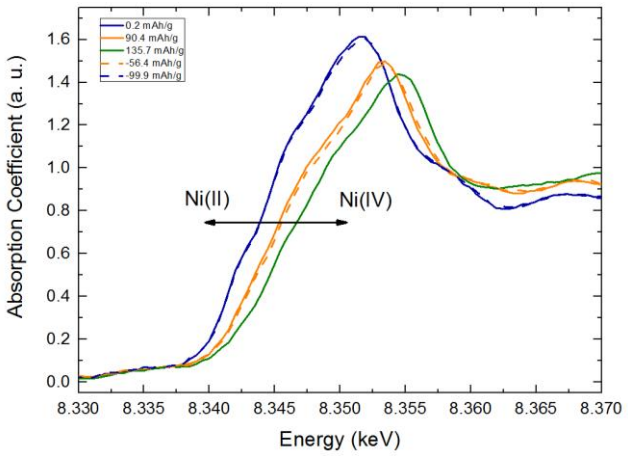

Fig.S4/ In-situ XANES spectra (Ni K-edge) of Mn15-900_700 at its maximal phase fraction during electrochemical cycling; solid line charge step, broken line discharge step.

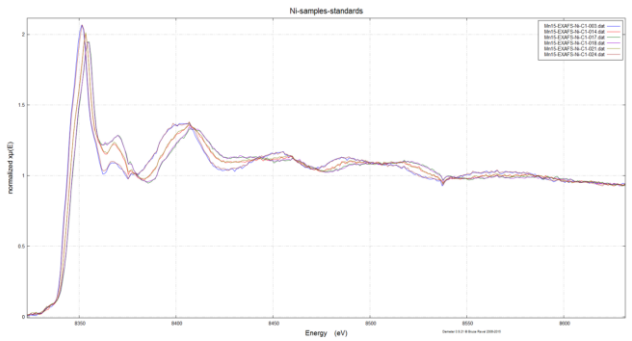

Fig.S5/ *In-situ EXAFS spectra at the Ni K-edge shown for the 3 distinct phases at the maximum phase fraction.*